COVER SHEET

NOTE: This conversheet is intended for you to list your article title and author(s) name only—this page will not appear on the CD-ROM.

Title: Parallel Adaptive Simulation of Weak and Strong Transverse-Wave Structures in H_2-O_2 Detonations

Authors: Ralf Deiterding

ABSTRACT

Two- and three-dimensional simulation results are presented that investigate at great detail the temporal evolution of Mach reflection sub-structure patterns intrinsic to gaseous detonation waves. High local resolution is achieved by utilizing a distributed memory parallel shock-capturing finite volume code that employs block-structured dynamic mesh adaptation. The computational approach, the implemented parallelization strategy, and the software design are discussed.

INTRODUCTION

The propagation of detonation waves in gaseous media is a complex multiscale phenomenon. While gaseous detonations propagate at supersonic velocities between 1500 and 2500 m/s, they inhibit non-negligible instationary sub-structures in the millimeter range. Transverse pressure waves propagate perpendicular to the detonation front forming triple points with enhanced chemical reaction. The hydrodynamic flow pattern in a triple point is a Mach reflection phenomenon under transient conditions. Depending on the local flow conditions, both double-Mach (aka "strong") and transitional Mach reflection ("weak") structures have been observed in experiments [1].

In the present paper, we discuss results from large-scale parallel simulations of Chapman-Jouguet (CJ) detonations in low-pressure hydrogen-oxygen with high argon dilution. In free space, the triple point movement in such mixtures is very regular leading to a repetitive trajectory pattern of regular "detonation cells". While the detailed hydrodynamic structure of such detonations has been fairly well analyzed by means of numerical simulation for two-dimensional rectangular channels and classified to be of double-Mach reflection type [2, 3], open questions remain for three space dimensions and non-rectangular geometries.

The paper is divided into a presentation of the computational methodology and a detailed discussion of computational results. We first summarize the employed finite volume discretization and discuss the used block-structured adaptive mesh refinement (SAMR) method from a software-oriented point of view. We then describe the domain decomposition based parallelization approach chosen in AMROC (Adaptive Mesh Refinement in Object-oriented C++) [4, 5], our freely available SAMR frame-

Ralf Deiterding, Oak Ridge National Laboratory, P.O. Box 2008 MS6367, Oak Ridge, TN 37831, U.S.A.

work, and give an overview of AMROC's object-oriented design. The second part of the paper presents high-resolution results of two- and three-dimensional simulations of regular cellular detonation structures in purely Cartesian geometry and two-dimensional computations of detonations propagating through smooth pipe bends. A detailed triple point analysis of weak and strong structures found in these simulations completes the analysis.

COMPUTATIONAL METHOD

The appropriate model for detonation propagation in premixed gases with realistic chemistry are the inviscid Euler equations for multiple thermally perfect species with reactive source terms [1, 6] that read

$$\begin{array}{rcrcl} \partial_t \rho_i & + & \nabla\cdot(\rho_i\vec{u}) & = & W_i\,\dot{\omega}_i\,, \\ \partial_t(\rho\vec{u}) & + & \nabla\cdot(\rho\vec{u}\otimes\vec{u})+\nabla p & = & 0\,, \\ \partial_t(\rho E) & + & \nabla\cdot((\rho E+p)\vec{u}) & = & 0\,, \end{array} \tag{1}$$

with $i = 1,\ldots,K$. Herein, ρ_i denotes the partial density of the ith species and $\rho = \sum_{i=1}^{K}\rho_i$ is the total density. The ratios $Y_i = \rho_i/\rho$ are called mass fractions. We denote the velocity vector by $\vec{u}$ and E is the specific total energy. We assume that all K species are ideal gases in thermal equilibrium and that the hydrostatic pressure is given as the sum of the partial pressures $p_i = \mathscr{R}T\rho_i/W_i$ with $\mathscr{R}$ denoting the universal gas constant and W_i the molecular weight, respectively. The evaluation of the last equation requires the previous calculation of the temperature T. As detailed chemical kinetics necessitate species with temperature-dependent material properties, each evaluation of T involves the approximate solution of an implicit equation by Newton iteration [7]. In here, the chemical production rates are modeled with a hydrogen-oxygen reaction mechanism extracted from the larger hydrocarbon mechanism by Westbrook [8] and considers the 9 species H, O, OH, H_2, O_2, H_2O, HO_2, H_2O_2 and Ar.

Finite volume scheme

We employ a time-operator splitting approach to decouple hydrodynamic transport and chemical reaction numerically. A semi-implicit Rosenbrock-Wanner method [9] is used to integrate the kinetics within each finite volume cell. Temperature-dependent material properties are derived from look-up tables that are constructed during start-up of the computational code. The expensive reaction rate expressions are evaluated by a mechanism-specific Fortran-77 function, which is produced by a source code generator on top of the Chemkin-II library in advance.

Since detonations involve supersonic shock waves, we use a finite volume discretization that achieves proper upwinding in all characteristic fields. The scheme utilizes a quasi-one-dimensional approximate Riemann solver of Roe-type and is extended to multiple space-dimensions via the method of fractional steps. Special corrections are applied to avoid unphysical total densities and internal energies near vacuum due to the Roe linearization, to ensure positive mass fractions, and to prevent the disastrous carbuncle phenomenon. The MUSCL[1]-Hancock variable extrapolation technique is employed to construct a second-order method. The upwind scheme including all modifications is detailed in [7, 10].

In order to consider geometrically complex moving boundaries within an originally Cartesian upwind method, we use some of the finite volume cells as ghost cells

[1] Monotone Upstream-centered Schemes for Conservation Laws

to enforce immersed boundary conditions [11]. Their values are set immediately before the original numerical update to model rigid embedded walls. The boundary geometry is mapped onto the Cartesian mesh by employing a scalar level set function ϕ that stores the signed distance function. A cell is considered to be an interior cell if the distance in the *midpoint* is positive and is treated as exterior otherwise. Beside the alteration of the values in the embedded ghost cells the numerical stencil by itself is not modified. Slight approximation errors due to this approach are alleviated by dynamic mesh adaptation. The detailed implementation of the immersed wall boundary conditions for system (1) is described in [10].

Adaptive mesh refinement

In order to supply the required temporal and spatial resolution efficiently, we employ the block-structured adaptive mesh refinement method after Berger and Collela [12], which is tailored especially for hyperbolic conservation laws on logically rectangular finite volume grids. Instead of replacing single cells by finer ones, as it is done in cell-oriented refinement techniques, the SAMR method follows a patch-oriented approach. Cells being flagged by various error indicators (shaded in Figure 1) are clustered with a special algorithm [13] into non-overlapping rectangular grids. Refinement grids are derived recursively from coarser ones and a hierarchy of successively embedded levels is thereby constructed (cf. Figure 1). All mesh widths on level l are r_l-times finer than on level $l-1$, i.e. $\Delta t_l := \Delta t_{l-1}/r_l$ and $\Delta x_{n,l} := \Delta x_{n,l-1}/r_l$ with $r_l \geq 2$ for $l > 0$ and $r_0 = 1$, and a time-explicit finite volume scheme (in principle) remains stable on all levels of the hierarchy. Note that the application of recursive time step refinement is a key difference between the SAMR approach and usual unstructured adaptation strategies.

The numerical scheme is applied on level l by calling a single-grid routine in a loop over all subgrids. The subgrids become computationally decoupled by employing additional ghost cells around each computational grid. Three types of ghost cells have to be considered in the sequential case (see Figure 2). Cells outside of the root domain are used to implement physical boundary conditions. Ghost cells overlaid by a grid on level l have a unique interior cell analogue and are set by copying the data value from the grid, where the interior cell is contained (synchronization). On the root level no further boundary conditions need to be considered, but for $l > 0$ also internal boundaries can occur. They are set by a conservative time-space interpolation from two previously calculated time steps of level $l-1$.

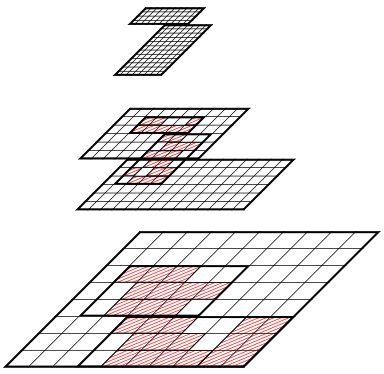

Figure 1. SAMR employs a hierarchy of successively embedded rectangular subgrids.

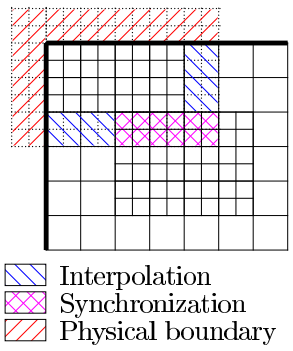

Figure 2. Sources of ghost cell values at the boundaries of an SAMR subgrid.

Beside a general data tree that stores the topology of the hierarchy, the SAMR method requires at most two regular arrays assigned to each subgrid. They contain the discrete vector of state for the actual and updated time step. The regularity of the data allows high performance on vector and super-scalar processors and cache optimizations. Small data arrays are effectively avoided by leaving coarse level data structures untouched when higher level grids are created. Values of cells covered by finer subgrids are overwritten by averaged fine grid values subsequently. This operation leads to a modification of the numerical stencil on the coarse mesh and requires a special flux correction in cells abutting a fine grid. The correction replaces the coarse grid flux along the fine grid boundary by a *sum* of fine fluxes and ensures the discrete conservation property of the hierarchical method at least for purely Cartesian problems without embedded boundaries. See [12] or [14] for details.

Parallelization

Up to now, various reliable implementations of the SAMR method for single processor computers have been developed [15, 16]. Even the usage of parallel computers with shared memory is straightforward because a time-explicit scheme allows the parallel calculation of the grid-wise numerical update [13]. But the question for an efficient parallelization strategy becomes more complex for distributed memory architectures. Due to the technical difficulties in implementing dynamical adaptive methods in distributed memory environments only few parallelization strategies have been considered in practice yet [17, 18].

In the AMROC framework, we follow a rigorous domain decomposition approach and partition the SAMR hierarchy from the root level on. We assume a parallel machine with P identical nodes and split the root domain G_0 into P non-overlapping portions G_0^p, $p = 1, \ldots, P$ by

$$G_0 = \bigcup_{p=1}^{P} G_0^p \quad \text{with} \quad G_0^p \cap G_0^q = \emptyset \ \text{ for } p \neq q \, .$$

The key idea now is that all higher level domains G_i are required to follow the decomposition of the root level, i.e.

$$G_l^p := G_l \cap G_0^p \, . \tag{2}$$

Condition (2) can cause the splitting of a subgrid $G_{l,m}$ into multiple subgrids on different processors. Under requirement (2) we estimate the work on an arbitrary subdomain $\Omega \subset G_0$ by

$$\mathscr{W}(\Omega) = \sum_{l=0}^{l_{\max}} \left[\mathscr{N}_l(G_l \cap \Omega) \prod_{\kappa=0}^{l} r_\kappa \right] \, . \tag{3}$$

Herein, $\mathscr{N}_l(\cdot)$ denotes the total number of FV cells on level l in the given domain. The product in (3) is used to consider the time step refinement. A nearly equal distribution of the work necessitates

$$\mathscr{L}^p := \frac{P \cdot \mathscr{W}(G_0^p)}{\mathscr{W}(G_0)} \approx 1 \quad \text{for all } p = 1, \ldots, P \, . \tag{4}$$

In AMROC, decompositions G_0^p with similar workload are found at runtime as the hierarchy evolves by a hierarchical partitioning algorithm based on a generalization of

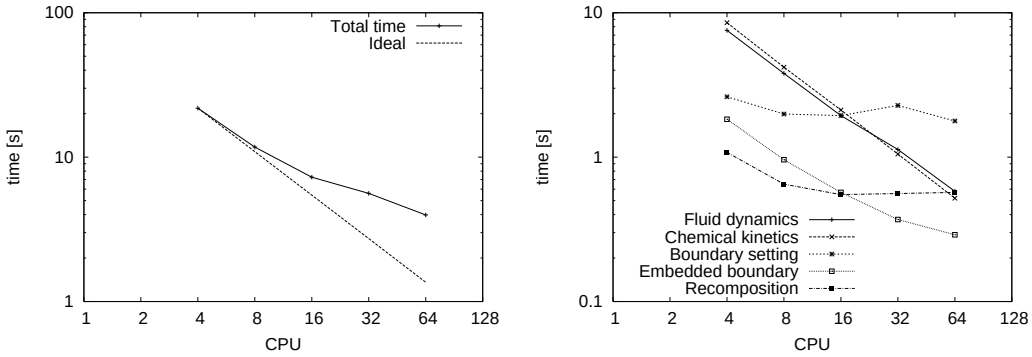

Figure 3. Strong scalability test for the two-dimensional chemically reactive SAMR code. Total time required for one full integration and refinement cycle (left) and for the most important operations (right).

Hilbert's space-filling curve [19]. The space-filling curve defines an ordered sequence on the cells of the root level that can easily be split in load-balanced portions. As such curves are constructed recursively, they are locality preserving and therefore avoid an excessive data redistribution overhead. Further on, the surface area is small, which reduces synchronization costs.

The advantage of the rigorous domain decomposition approach is that it is comparably easy to implement, with hierarchy recomposition and subgrid synchronization being the only parallel operations [20], and overall work is well balanced. However, the work on each levels is not perfectly distributed, which causes slight delays during subgrid synchronization (in operation *Boundary setting*). We have found the approach well suited for parallel three-dimensional computations on up to a few hundreds CPUs.

Results from a two-dimensional scalability test are depicted in Figure 3. The simulation approximates the shock-induced combustion around a sphere that travels at supersonic speed through a hydrogen-oxygen-argon mixture [10]. The computation is carried out in the frame of reference of the body, leading to a steady flow field, and uses a base mesh of only 70×40 cells and 3 additional levels refined by a factor of 2. The test was run on a cluster of Intel Xeon 3.4 GHz dual-processors connected with a Gigabit-Ethernet network. As can be inferred from the right graphic of Figure 3, the numerical single-block operations for fluid dynamics and chemical kinetics update scale linearly, however, the expense of the communication-dependent operations for synchronization and hierarchy recomposition remains basically constant for larger CPU counts.

Object-oriented implementation

In block-structured dynamically adaptive codes, three abstraction levels can be identified. At the top level, a particular physical simulation problem is formulated by providing a finite volume scheme, by setting boundary and initial conditions, and by specifying interpolation (prolongation) and averaging (restriction) methods for the inter-level transfer operations. Characteristic of block-structured methods is that at this level only single-patch routines need to be provided. In AMROC, SAMR implementation classes call the single-patch routines through abstract class interfaces. For a fully implemented SAMR algorithm, the system is used as an application framework invoked by a generic main program. Classes implementing SAMR algorithms

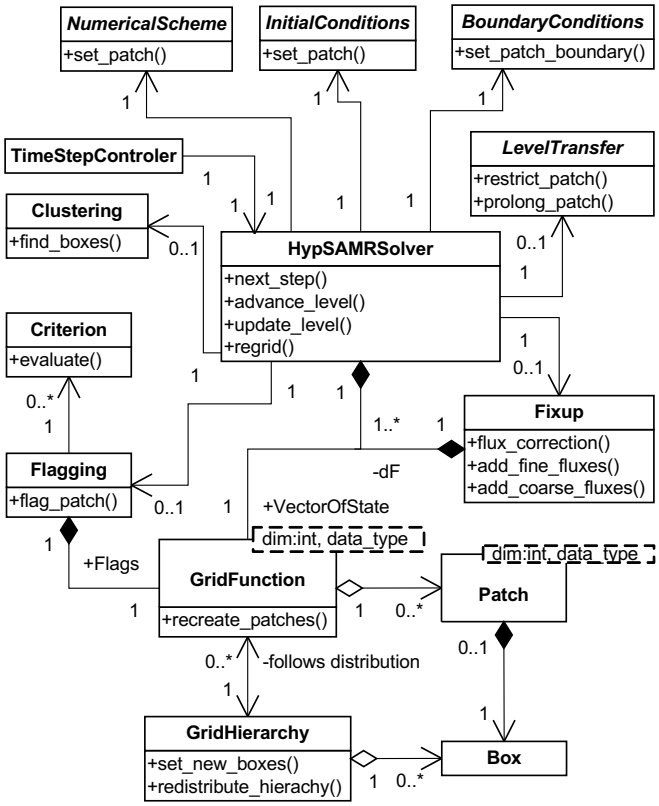

Figure 4. UML class diagram for the most important AMROC components implementing the Cartesian Berger-Collela-type SAMR method.

and their auxiliary components operating on and manipulating complex hierarchical data make up the second level. In AMROC, components such as the flagging of cells for refinement depending on various criteria, the clustering of flagged cells into rectangular regions, inter-level data transfer and flux correction (fixup) reside in clearly separated classes. This is highlighted in Figure 4 which displays the most important AMROC classes and their relationships in Unified Modeling Language (UML) notation [21] for the purely Cartesian case. The recursive Berger-Collela SAMR algorithm tailored for the hyperbolic problems of interest here is realized in the central class *HypSAMRSolver*; all others classes are generic, enabling the utilization of AMROC as a software framework for the efficient implementation of different SAMR algorithms typically implemented in new central SAMRSolver classes.

The intermediate AMROC design level naturally utilizes classes of the base level that provides hierarchical data structures. The base level is divided into elementary functionality for single grid patches and the implementation of various lists that store these patches hierarchically. A common design for the base level (see also [17]) involves a *Box* class to specify a single rectangular box in global integer index space. Methods for geometric operations on boxes like concatenation or intersection are available. A *Patch* class adds consecutive data storage to a Box. In AMROC, the geometrical description of all refinement areas is stored in hierarchical lists of Box objects inside a single *GridHierarchy*. The templatized class *GridFunction* creates Patch objects for various, possibly complex, data types according to the Box lists of GridHierarchy. As the refinement lists in GridHierarchy evolve and are dynamically

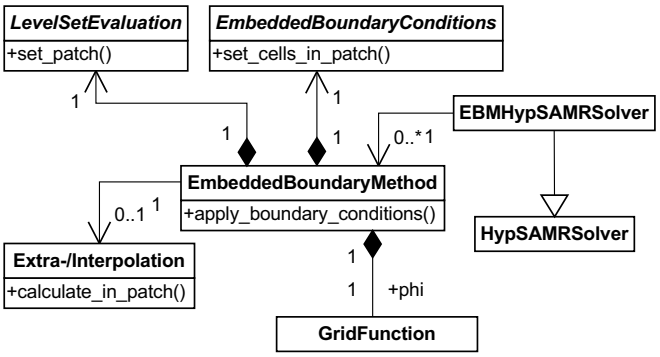

Figure 5. Extension of Figure 4 for level-set-based embedded boundary methods.

distributed to an evolving set of processors, the Patch objects in GridFunction are automatically re-created, including parallel redistribution and synchronization.

The design of the hierarchical data structures in AMROC is based on the DAGH (Distributive Adaptive Grid Hierarchies) package by Parashar and Browne [18] that itself was intended as software framework for SAMR methods, however, the complexity of the algorithms and their auxiliary components makes framework concepts at higher design levels more effective. As an illustration, Figure 5 shows the most important classes that have been added to the originally Cartesian SAMR framework to implement level-set-based embedded boundary methods. An abstract class *LevelSetEvaluation* is provided to evaluate the scalar GridFunction ϕ patch-wise; *EmbeddedBoundaryConditions* allows the specification of the detailed boundary value modification. Multiple EmbeddedBoundaryMethods can also be considered and are incorporated with minimal implementation overhead into the existing algorithms of the SAMRSolver class for hyperbolic problems, HypSAMRSolver, through the derived class *EBMHypSAMRSolver*. The only operation that had to be extended was that of applying physical boundary conditions.

RESULTS

The classical Zel'dovich-von Neumann-Döring (ZND) theory (cf. [1] or [14]) predicts the internal structure of a self-sustained one-dimensional stationary detonation wave. However, the energetic interplay between the leading hydrodynamic shock wave and the subsequent combustion region is inherently unstable and already early experiments, e.g. [22], uncovered that the reduction to one space dimension is not even justified in long combustion devices. The multi-dimensional instability manifests itself in instationary shock waves propagating perpendicular to the detonation front. A complex Mach reflection pattern is formed downstream of each triple point, where the detonation front is intersected by a transverse shock.

Regular cellular detonation structure in 2D

Self-sustained detonations in low-pressure hydrogen-oxygen-argon mixtures are known to produce very regular triple point movements [22]. The triple point trajectories form regular "fish-scale" patterns, so called detonation cells, with a characteristic length L and width λ, that depend primarily on the energy release intrinsic to the mixture.

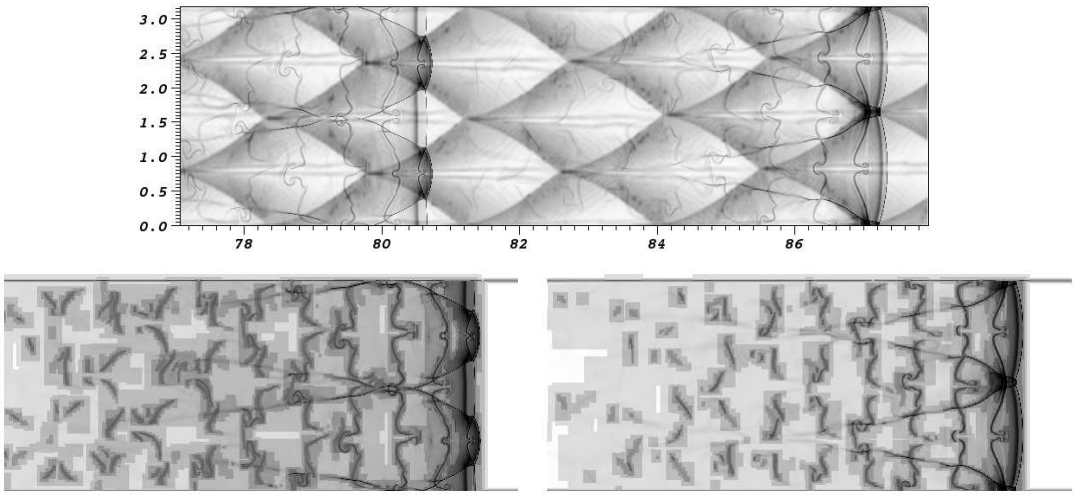

Figure 6. Detonation front on triple point tracks (top) in a rectangular channel of 3.2 cm width, $H_2 : O_2 :$ Ar mixture of molar ratios 2:1:7 at initially 298 K and 10 kPA. Lower row: Schlieren plots of the density on the refinement levels (gray) visualize the dynamic mesh adaptation.

Two snapshots from the simulation of regular oscillating transverse waves in a CJ detonation in two space dimensions are depicted in Figure 6. The mixture is $H_2 : O_2 :$ Ar of molar ratios 2:1:7 at initially 298 K and 10 kPA for which our computations with the Westbrook mechanism [8] predict a detonation velocity of $d_{CJ} = 1638.5\,\mathrm{m/s}$. The computation is initialized with the ZND solution; transverse disturbances are initiated by placing a small rectangular unreacted pocket behind the detonation front [2, 14]. After simulating several hundred micro-seconds of physical time, the periodic oscillation is clearly established.

The results shown in Figure 6 were carried out in an Eulerian frame of reference with a long channel of $1.0\,\mathrm{m} \times 3.2\,\mathrm{cm}$. The base mesh was 2000×128 and four additional levels of Cartesian mesh adaptation with refinement factors 2, 2, 2, and 4 were used giving an effective resolution of 67.6 Pts within the half reaction length, l_{ig}, the distance between shock and reaction zone according to ZND theory. Mesh adaptation is based on a physically motivated combination of scaled gradients of ρ and p and error estimation by Richardson extrapolation of the mass fractions Y_i (see [10] for details). The upper graphic of Figure 6 displays triple point trajectories in a part of the computational domain with the detonation front at two points in time overlaid. The trajectories are visualized by tracking the maximum of the magnitude of the vorticity on a uniform auxiliary grid with the mesh widths of level 1. The bottom row of Figure 6 shows the dynamic mesh for the two time steps.

An enlargement of the detonation structure in Figure 7 shortly before the collision of two triple points shows clearly that the shock wave pattern around each triple point is of double-Mach reflection (DMR) or strong type. The essential regions around a triple point in Figure 7 are: inflow (A), Mach stem (B), transverse wave (C), and incident shock (D). Regions B and C are separated by the slip line, a contact discontinuity. Characteristic for the DMR pattern is a high supersonic velocity in region C that leads to the formation of a further shock creating a secondary triple point on the transverse wave. In Figure 7, this secondary shock separates regions C and E. The very weak slip line, emanating from the secondary triple point between regions E and F, can hardly be inferred.

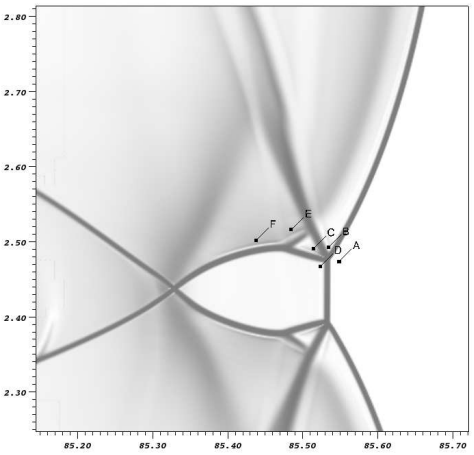

Figure 7. Left: Schlieren image of clearly established DMR pattern shortly before next the triple point collision, $S = 0.653$.

TABLE I. STATES IN FIGURE 7.

	p/p_A	ρ/ρ_A	T [K]	v[m/s]	M
A	1.00	1.00	298	1775	5.078
B	31.45	4.17	2248	447	0.477
C	31.69	5.32	1775	965	1.153
D	19.17	3.84	1487	1178	1.533
E	35.61	5.72	1856	901	1.053
F	40.61	6.09	1987	777	0.880

In order to analyze a Mach reflection pattern quantitatively it is necessary to map the velocity field of the simulation into a frame of reference attached to the triple point. However, the reliable estimation of the triple point speed v_0 from a single time step is non-apparent. When evaluating v_0 we take advantage of the fact that the triple point is formed at the tip, where the Mach stem intersects the incident region, and that the oblique shock relations [23, 24] between two points in regions A and B close to the triple point must hold true. We only require the two relations

$$\rho_A v_A \sin(\phi_B) = \rho_B v_B \sin(\phi_B - \theta_B) \,, \tag{5}$$

$$p_A + \rho_A v_A^2 \sin^2(\phi_B) = p_B + \rho_B v_B^2 \sin^2(\phi_B - \theta_B) \,. \tag{6}$$

Inserting Eq. (5) into Eq. (6) allows the elimination of $v_B \sin(\phi_B - \theta_B)$, which yields

$$v_A = \frac{1}{\sin\phi_B} \sqrt{\frac{\rho_B(p_B - p_A)}{\rho_A(\rho_B - \rho_A)}} \,.$$

As the gas is initially at rest, the triple point velocity is $v_0 = -v_a$ and ϕ_B, the angle of inflow, is given as the angle between Mach stem front and the triple point trajectory, which can be measured from visualizations comparable to the upper graphic of Figure 6. The states close of the triple point of Figure 7 are given Table I. Since the triple point is far ahead of the reaction region (the diffused downstream front in Figure 7), changes in mixture are neglected in evaluating the Mach number M in the triple point pattern. As it can be expected in a DMR [24], M_C is clearly greater than 1. A further important quantity for triple point structures is the strength S of the transverse wave [1] that is defined as

$$S := \frac{p_C - p_D}{p_D} \,. \tag{7}$$

For the present computation, S decreases throughout one regular detonation cell from ~ 1.05 to ~ 0.65 which indicates clearly that only the strong or DMR structure occurs.

Detonation structure in smooth pipe bends in 2D

In order to study triple point structures under transient conditions, we simulate the propagation of the regularly oscillating detonation through smooth pipe bends

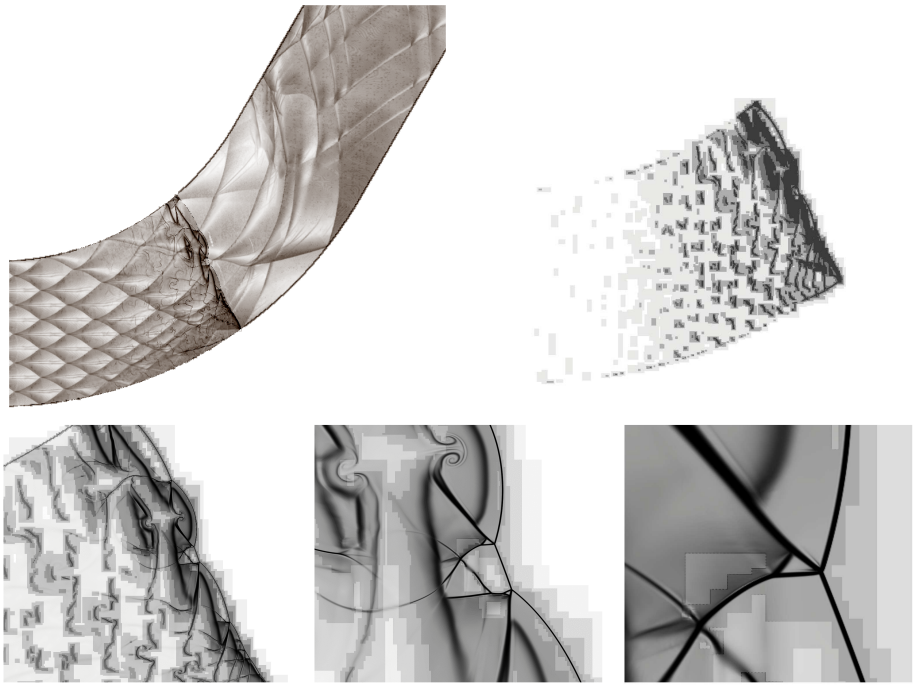

Figure 8. Schlieren plot of density on triple point tracks (upper left) and on refinement regions (shaded gray, upper right and lower row) for $\varphi = 60^{\circ}$ after $t = 150\,\mu$s simulated time. Several enlargement steps are necessary to visualize the secondary triple point structure captured by the adaptive computation.

of varying angles. Particularly for low initial pressures, and therefore larger cellular structures, detonation propagation through bends is rather complex. For small radius and larger bending angle, the detonation wave structure is not maintained and triple point quenching can be observed at the outer compressive side, while detonation failure and violent re-initiation occur at the inner diffractive wall (see Figure 5a of [25]).

Again, we choose for our study $H_2 : O_2 : Ar/2 : 1 : 7$ at 298 K and 10.0 kPa, for which one-dimensional ZND theory would predict a maximal pressure of ~ 270 kPa. The computations are initialized by reproducing the snapshot of a single detonation cell with $\lambda \approx 1.6$ cm periodically with the detonation front approximately 13 cm before the beginning of the curved section. To accommodate a reduction of the induction length when the detonation wave gets compressed, all computations again use an effective resolution of $67.6\,\mathrm{Pts}/l_{\mathrm{ig}}$, which is achieved by four additional levels of Cartesian mesh adaptation with refinement factors 2, 2, 2, and 4. For instance, for bend angle $\varphi = 60^{\circ}$, with a base mesh of 1200×992 cells, the adaptive computation uses approximately 7.1 M to 3.4 M cells on all and 4.8 M to 1.8 M cells on the highest level instead of $\sim 1,219$ M in the uniform case. The calculations were run on 64 Intel Xeon 2.4 GHz dual-processor nodes with Quadrics interconnect and required nevertheless $\sim 70,000$ h CPU each (~ 23 days wall time). The extraordinary high efficiency in capturing only the essential features near the detonation front is illustrated in Figure 8, in which the characteristic DMR pattern (cf. Figure 6) is clearly resolved.

Large-scale flow features are best understood by looking at the history of the triple point trajectories displayed in Figure 9. At the outer wall, the detonation becomes accelerated as the leading shock front undergoes Mach reflection. Along the inner wall, shock wave diffraction causes a continuous pressure decrease that results in a

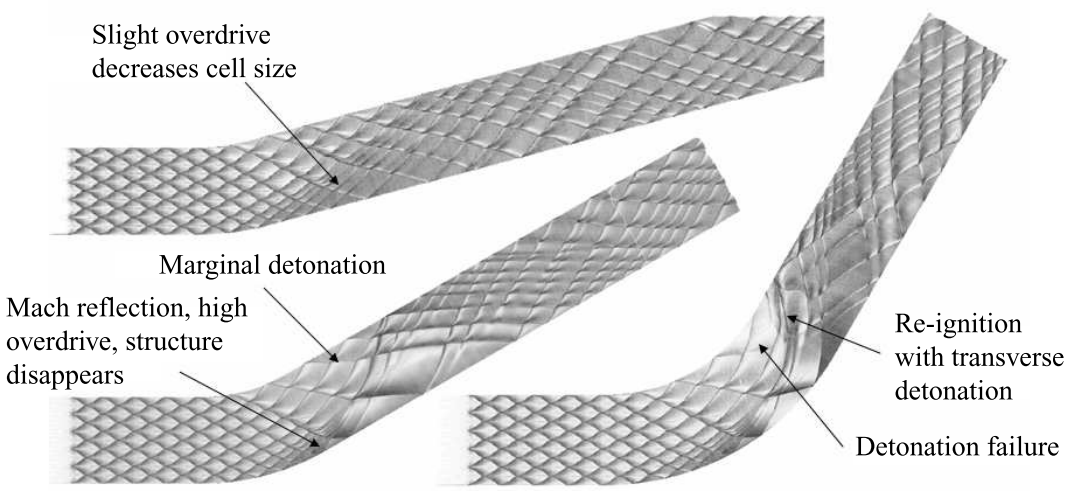

Figure 9. Triple point tracks for $\varphi = 15^{\circ}$ (left, top), $\varphi = 30^{\circ}$ (left, bottom), and $\varphi = 60^{\circ}$ (right).

slight temporary increase in detonation cell size for a bending angle of $\varphi = 15^{\circ}$, in a transmitted marginal detonation close to the limit of detonability for $\varphi = 30^{\circ}$, and in temporary detonation failure for $\varphi \geq 45^{\circ}$. For $\varphi \geq 30^{\circ}$, the appearance of unreacted pockets behind the marginal detonation wave can also be observed (see Figure 8).

Diffraction and compression of the detonation wave at the bend also lead to changes of the transverse wave strength S. While the state behind the transverse wave C remains initially largely unchanged, the change in geometry alters the incident state D. Near the inner bend wall, the incident pressure p_D drops, leading to a considerable increase in S. The resulting triple point structure, as depicted in Figure 10, is of DMR type, but note that the chemical reaction across the transverse wave is visibly enhanced and M_c is considerably increased (compare Figure 7 and Table I). In the compression region near the outer wall, however, p_D increases drastically leading to a considerable decrease of S. As a consequence, the flow in region C decelerates. The secondary shock between C and E is no longer necessary for a stable configuration and the triple point now exhibits a transitional Mach reflection (TMR) or weak pattern (cf. Figure 11). Characteristic for the TMR structure is that the flow in region C is just barely supersonic [24]. A TMR structure is also exhibited in the diffraction region when a sufficiently large angle φ causes detonation failure. As the leading shock and the reaction zone decouple, especially p_C decreases and the wave strength S declines. The exhibited pattern close to triple point failure is again the TMR type (see Figure 12).

For the completely transmitted marginal case ($\varphi = 30^{\circ}$), the transition back to a regular oscillation is initiated by a strong triple point originating in the region of detonation Mach reflection. For the configurations with $\varphi \geq 45^{\circ}$, in which additionally partial detonation failure occurs, the transverse re-initiation wave itself becomes a detonation. This interesting situation is depicted in Figure 13. The DMR pattern formed at the detonation front is extremely strong; further on, an instationary triple point arises on the transverse detonation itself that propagates toward the detonation front. Very high pressures occur in states J and K behind the transverse wave of this triple point. When it hits the inner wall, the simulation's maximal pressure value of 3.4 MPa does arise. For $\varphi = 60^{\circ}$, a smaller peak pressure is reached as the critical triple point merges with the primary triple point before wall contact. Note that com-

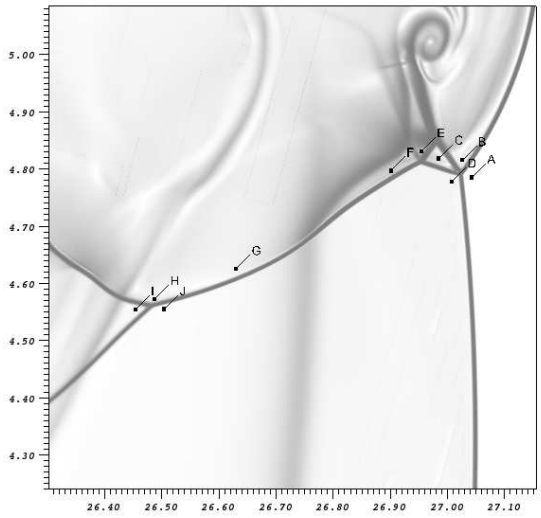

	p/p_A	r/r_A	T [K]	v[m/s]	M
A	1.00	1.00	298	1835	5.249
B	33.77	4.33	2326	447	0.469
C	33.12	5.80	1701	1111	1.355
D	16.06	3.67	1304	1363	1.889
E	66.90	9.10	2191	758	0.818
F	57.94	7.64	2259	668	0.710
G	35.28	3.41	3235	699	
H	38.98	3.41	3589	593	
I	23.66	2.37	3149	969	
J	13.58	1.67	2570	1347	

Figure 10. Strong DMR structure in diffraction region behind bend, $\varphi = 15$, $S = 1.062$.

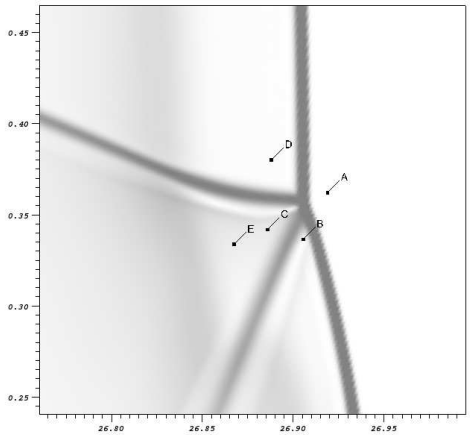

	p/p_A	r/r_A	T [K]	v[m/s]	M
A	1.00	1.00	298	1908	5.459
B	34.14	4.21	2418	647	0.666
C	35.49	4.95	2135	929	1.015
D	26.53	4.09	1934	1085	1.243
E	34.91	4.88	2134	938	1.025

Figure 11. TMR structure in compression region shortly behind bend, $\varphi = 15$, $S = 0.338$.

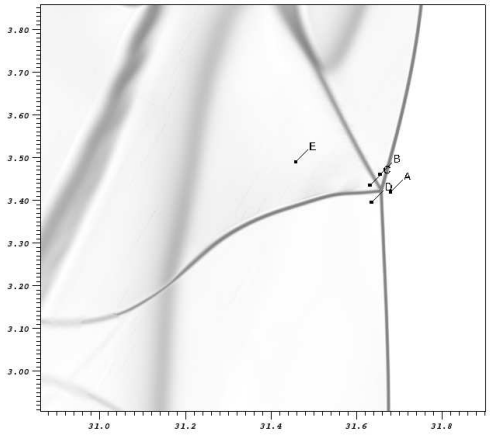

	p/p_A	r/r_A	T [K]	v[m/s]	M
A	1.00	1.00	298	1424	4.073
B	18.97	3.83	1475	502	0.656
C	18.73	4.30	1297	726	1.009
D	14.00	3.58	1167	848	1.240
E	19.08	4.20	1352	744	1.014

Figure 12. TMR structure in marginal region near limit of detonability, $\varphi = 30$, $S = 0.338$.

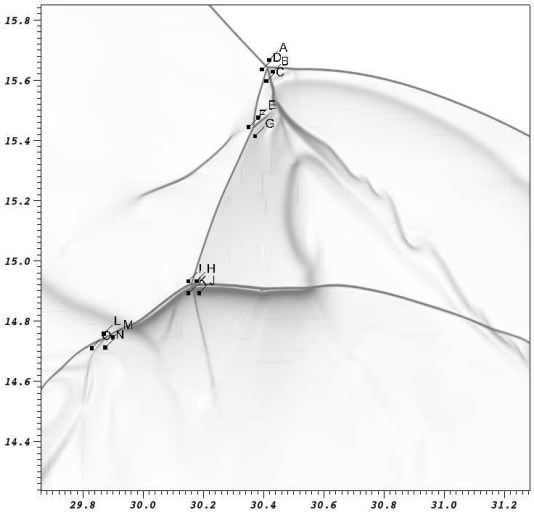

	p/p_A	r/r_A	T [K]	v[m/s]	M
A	1.00	1.00	298	1812	5.186
B	32.58	4.27	2272	456	0.483
C	33.23	6.21	1594	1156	1.454
D	13.98	3.58	1162	1446	2.119
E	31.54	6.30	1492	1208	1.569
F	16.13	4.14	1161	1393	2.042
G	41.63	7.45	1665	1034	1.274
H	30.57	6.31	1443	1180	1.557
I	14.11	3.85	1092	1431	2.161
J	77.31	9.08	2610	756	
K	78.85	8.59	2812	521	

Figure 13. Re-ignition with strong DMR and transverse detonation, $\varphi = 45$, $S = 1.377$.

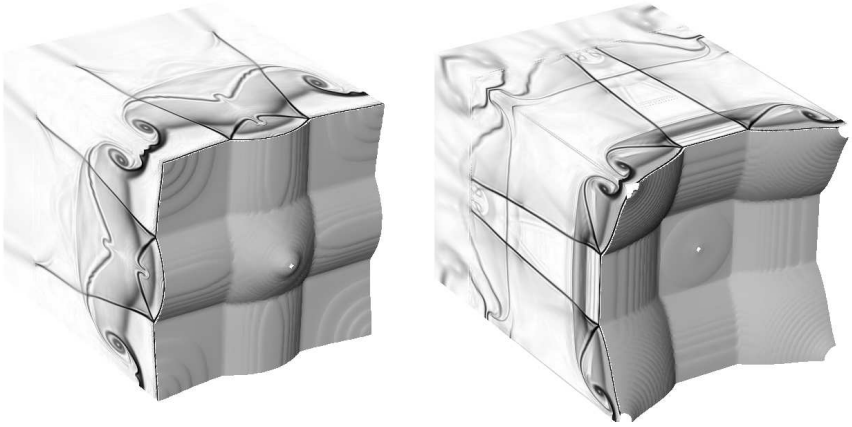

Figure 14. Schlieren planes of the density in the first (left, $S \approx 0.36$) and second (right, $S \approx 0.42$) half of a detonation cell. Data displayed is for $5.0\,\mathrm{cm} < x_1 < 7.0\,\mathrm{cm}$ and mirrored at $x_2, x_3 = 0$.

putations on significantly coarser meshes, that fail to resolve the detonation structure evolution accurately, are inherently unable to predict the re-ignition event correctly and therefore severely underestimate the pressure maximum.

Regular cellular detonation structure in 3D

While it is nowadays feasible to investigate the evolution of fully resolved detonation structures in realistic two-dimensional geometries (see above), three-dimensional simulations are still restricted to elementary situations. As an example we show results from a simulation to analyze the detailed triple point structure for a CJ detonation in $H_2 : O_2 : Ar/2 : 1 : 7$ at initially 298 K and pressure 6.67 kPa. The detonation cell width in free space is $\lambda \approx 3.0\,\mathrm{cm}$ [2, 3] and the ZND induction length $l_{ig} \approx 1.4\,\mathrm{mm}$. Previous numerical studies [26, 14] have confirmed that this width is identical in two and three space dimensions. In rectangular three-dimensional domains, the triple points manifest as orthogonal triple point lines [27], cf. Figure 14. A detailed hydrodynamic analysis uncovers that, although the detonation velocity is unaltered, the fluctuations in pressure, temperature, and therefore induction length are considerably larger than in the two-dimensional case [28]. We show results from a highly resolved computation in a frame of reference attached to the detonation front. The domain has the dimensions $[0\,\mathrm{cm}, 10\,\mathrm{cm}] \times [0\,\mathrm{cm}, 1.5\,\mathrm{cm}] \times [0\,\mathrm{cm}, 1.5\,\mathrm{cm}]$ to simulate exactly 1/4 of a regular detonation cell. A constant inflow with $-d_{CJ} = 1626.9\,\mathrm{m/s}$ is applied at the right, outflow conditions at the left boundary. Symmetry boundary conditions are used at all other sides.

The computation uses a base mesh of $400 \times 24 \times 24$ and two additional levels of mesh adaptation with refinement factors 2, 4 giving an effective resolution of $44.8\,\mathrm{Pts}/l_{ig}$. Refinement criteria are chosen similarly as before, where all refinement flags are overall deleted in the range $0\,\mathrm{cm} < x_1 < 4\,\mathrm{cm} + wt$ with $w := 20\,\mathrm{m/s}$. To ensure a perfectly regular oscillation the computation is run for 7318 root level time steps with $C_{CFL} \approx 0.95$ to $t_e = 800\,\mu\mathrm{s}$. After a simulation time of $\approx 600\,\mu\mathrm{s}$ a regular cellular oscillation with identical strength in x_2- and x_3-direction can be observed, cf. Figure 14. Note that in Figure 14 the data was mirrored twice to display a full detonation cell. The exhibited three-dimensional mode of propagation of two transverse

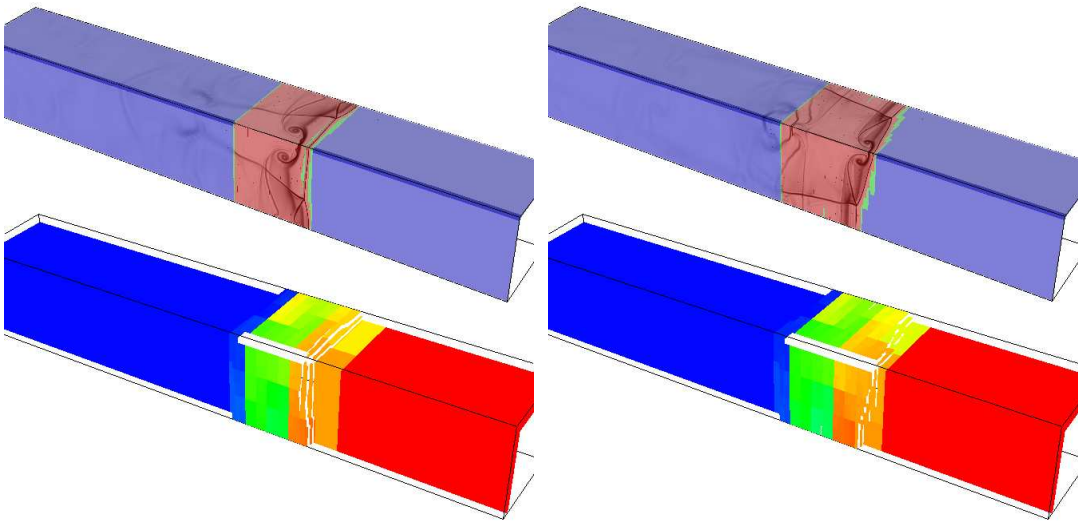

Figure 15. Schlieren plot of the density on refinement levels and domain distribution to 128 CPU (indicated by color) for the two time steps shown in Figure 14.

wave lines in perfect phase has also been found in experiments [29]. While previous investigations [26, 14] confirmed that our numerical approach is capable of capturing the transverse wave oscillation well on three to four times coarser meshes, the present computation also resolves secondary flow features. It allows the unambiguous classification of the triple point pattern displayed in the schlieren planes of the left graphic of Figure 14 as a TMR pattern with $S \approx 0.36$; the transverse wave strength of the pattern shown in the planes of the right image is ~ 0.42. Note that the regularly oscillating two-dimensional case discussed previously exhibits only much lager values of S and therefore only the DMR pattern occurs.

The 3D computation was run on 32 nodes of a Compaq AlphaServer quad-core system with high-speed Quadrics interconnect at Los Alamos National Laboratories and required $\sim 51,000$ h CPU, which corresponds to ~ 16.6 days wall time. A breakdown of the time in Table II confirms the good parallel efficiency of the implementation even for larger problems. The adaptive computation uses approximately 16.5 M cells on average instead of ~ 118 M in the uniform case, cf. upper row of Figure 15. The lower row of Figure 15 visualizes by different color the domain decompositions of the evolving hierarchy to 128 CPU with the refinement levels elevated. These pictures illustrate the good stability of our partitioning methodology for small changes in the workload.

TABLE II. BREAKDOWN OF THE COMPUTE TIME FOR THE 3D SIMULATION.

Task	%
Fluid dynamics	37.6
Chemical kinetics	25.1
Boundary setting	24.4
Recomposition	6.6
Misc.	6.3
Total [h CPU]	$\sim 51,000$

CONCLUSIONS

We have described the parallelization and implementation of a dynamically adaptive Cartesian finite volume method for simulating detonations in realistic gas mixtures with great accuracy. High local resolution is mandatory in physically relevant detonation simulations to accurately resolve the hydrodynamic sub-structures around triple points that are intrinsic to detonations in combustible gas mixtures. While the savings from dynamic mesh adaptation are necessarily moderate for simulations in a Galilean frame of reference, they have been demonstrated to be enormous for Eulerian settings. Large-scale adaptive two-dimensional structure simulations in pipe bends have been demonstrated to exhibit reductions of the finest mesh size of at least a factor of 250 and up to 680.

Utilizing the high resolution results provided by these computations, exemplary triple point structures have been quantitatively analyzed at the scale of secondary triple points. It is found that under transient geometric conditions an entire spectrum of weak transitional Mach to very strong double-Mach reflection patterns occurs. The type of Mach reflection exhibited seems to be primarily determined by the strength of the transverse wave S as defined in Eq. (7). This observation is confirmed by an exemplary high-resolution three-dimensional computation that shows lower values for S and therefore a transition to TMR rather than the DMR pattern as in the two-dimensional case. This result also indicates that fully predictive detonation simulations in generally will have to be carried out in three space dimensions. Since it was demonstrated that parallel capacity computing systems nowadays permit the accurate computation of detonation waves in technically relevant two-dimensional devices and the study of idealized three-dimensional configurations, this ultimate goal might already be attainable on available petaFLOPS supercomputers.

ACKNOWLEDGMENTS

This work is sponsored by the Office of Advanced Scientific Computing Research; U.S. Department of Energy (DOE) and was performed at the Oak Ridge National Laboratory, which is managed by UT-Battelle, LLC under Contract No. DE-AC05-00OR22725. The presented computations have been carried out while the author was at the California Institute of Technology and was supported by the ASC program of the Department of Energy under subcontract No. B341492 of DOE contract W-7405-ENG-48.

REFERENCES

1. Fickett, W. and W. C. Davis. 1979. *Detonation*. University of California Press, Berkeley and Los Angeles, CA.
2. Oran, E. S., J. W. Weber, E. I. Stefaniw, M. H. Lefebvre, and J. D. Anderson. 1998. "A numerical study of a two-dimensional H_2-O_2-Ar detonation using a detailed chemical reaction model," *Combust. Flame*, 113:147–163.
3. Hu, X. Y., B. C. Khoo, D. L. Zhang, and Z. L. Jiang. 2004. "The cellular structure of a two-dimensional H_2/O_2/Ar detonation wave," *Combustion Theory and Modelling*, 8:339–359.
4. Deiterding, R. 2002. "AMROC - Blockstructured Adaptive Mesh Refinement in Object-oriented C++," available at http://amroc.sourceforge.net.
5. Deiterding, R., R. Radovitzki, S. Mauch, F. Cirak, D. J. Hill, C. Pantano, J. C. Cummings, and D. I. Meiron. 2006. "Virtual Test Facility: A virtual shock physics facility for simulating the dynamic response of materials," available at http://www.cacr.caltech.edu/asc.

6. Williams, F. A. 1985. *Combustion theory*. Addison-Wesley, Reading, MA.
7. Deiterding, R. and G. Bader. 2005. "High-resolution simulation of detonations with detailed chemistry," in *Analysis and Numerics for Conservation Laws*, G. Warnecke, editor, Springer, pp. 69–91.
8. Westbrook, C. K. 1982. "Chemical kinetics of hydrocarbon oxidation in gaseous detonations," *Combust. Flame*, 46:191–210.
9. Kaps, P. and P. Rentrop. 1979. "Generalized Runge-Kutta methods of order four with stepsize control for stiff ordinary differential equations," *Num. Math.*, 33:55–68.
10. Deiterding, R. 2009. "A parallel adaptive method for simulating shock-induced combustion with detailed chemical kinetics in complex domains," *Computers & Structures*, 87:769–783.
11. Fedkiw, R. P., T. Aslam, B. Merriman, and S. Osher. 1999. "A non-oscillatory Eulerian approach to interfaces in multimaterial flows (the ghost fluid method)," *J. Comput. Phys.*, 152:457–492.
12. Berger, M. and P. Colella. 1988. "Local adaptive mesh refinement for shock hydrodynamics," *J. Comput. Phys.*, 82:64–84.
13. Bell, J., M. J. Saltzman, and M. Welcome. 1994. "Three-dimensional adaptive mesh refinement for hyperbolic conservation laws," *SIAM J. Sci. Comp.*, 15(1):127–138.
14. Deiterding, R. 2003. *Parallel adaptive simulation of multi-dimensional detonation structures*. PhD thesis, Brandenburgische Technische Universität Cottbus.
15. Berger, M. and R. LeVeque. 1998. "Adaptive mesh refinement using wave-propagation algorithms for hyperbolic systems," *SIAM J. Numer. Anal.*, 35(6):2298–2316.
16. Crutchfield, W. and M. L. Welcome. 1993. "Object-oriented implementation of adaptive mesh refinement algorithms," *J. Scientific Programming*, 2:145–156.
17. Rendleman, C. A., V. E. Beckner, M. Lijewski, W. Crutchfield, and J. B. Bell. 2000. "Parallelization of structured, hierarchical adaptive mesh refinement algorithms," *Computing and Visualization in Science*, 3.
18. Parashar, M. and J. C. Browne. 1997. "System engineering for high performance computing software: The HDDA/DAGH infrastructure for implementation of parallel structured adaptive mesh refinement," in *Structured Adaptive Mesh Refinement Grid Methods*, IMA Volumes in Mathematics and its Applications, Springer.
19. Parashar, M. and J. C. Browne. 1996. "On partitioning dynamic adaptive grid hierarchies," in *Proc. of the 29th Annual Hawaii Int. Conf. on System Sciences*, January 1996.
20. Deiterding, R. 2005. "Construction and application of an AMR algorithm for distributed memory computers," in *Adaptive Mesh Refinement - Theory and Applications*, volume 41 of *Lecture Notes in Computational Science and Engineering*, T. Plewa, T. Linde, and V. G. Weirs, eds. Springer, pp. 361–372.
21. Booch, G., J. Rumbaugh, and I. Jacobsen. 1999. *The unified modeling language user guide*. Addison-Wesley, Reading, MA.
22. Strehlow, R. A. 1968. "Gas phase detonations: Recent developments," *Combust. Flame*, 12(2):81–101.
23. Liepmann, H. W. and A. Roshko. 1957. *Elements of Gasdynamics*. Dover Publications, Inc., Mineola, NY.
24. Ben-Dor, G. 2007. *Shock wave reflection phenomena*. Springer-Verlag, Berlin, Heidelberg, 2nd edition.
25. Thomas, G. O. and R. L. Williams. 2002. "Detonation interaction with wedges and bends," *Shock Waves*, 11:481–492.
26. Deiterding, R. 2009. "Dynamically adaptive simulation of regular detonation structures using the Cartesian mesh refinement framework AMROC," *Int. J. Computational Science Engineering*, in press.
27. Williams, D. N., L. Bauwens, and E. S. Oran. 1997. "Detailed structure and propagation of three-dimensional detonations," *Proc. of the Combustion Institute*, 26:2991–2998.
28. Deiterding, R. 2003. "Numerical structure analysis of regular hydrogen-oxygen detonations," in *Proc. of Fall Meeting of Western States Section*. The Combustion Institute, October 21-23, 2003.
29. Hanana, M., M. H. Lefebvre, and P. J. Van Tiggelen. 1999. "Pressure profiles in detonation cells with rectangular or diagonal structure," in *Proc. of 17th Int. Colloquium on the Dynamics of Explosive and Reactive Systems*, Heidelberg, July 1999.